ACS APPLIED MATERIALS & INTERFACES

www.acsami.org

Research Article

Solvent-Free UV Polymerization of *n*-Octadecyl Acrylate in Butyl Rubber: A Simple Way to Produce Tough and Smart Polymeric Materials at Ambient Temperature

Esra Su, Cigdem Bilici, Gozde Bayazit, Semra Ide, and Oguz Okay*

Cite This: *ACS Appl. Mater. Interfaces* 2021, 13, 21786–21799

Read Online

ACCESS | Metrics & More | Article Recommendations | Supporting Information

ABSTRACT: One of the most fascinating challenges in recent years has been to produce mechanically robust and tough polymers with smart functions such as self-healing and shape-memory behavior. Here, we report a simple and versatile strategy for the preparation of a highly tough and highly stretchable interconnected interpenetrating polymer network (c-IPN) based on butyl rubber (IIR) and poly(*n*-octadecyl acrylate) (PC18A) with thermally induced healing and shape-memory functions. Solvent-free UV polymerization of *n*-octadecyl acrylate (C18A) at 30 ± 2 °C in the presence of IIR leads to IIR/PC18A c-IPNs with sea-island or co-continuous morphologies depending on their IIR contents. The lamellar crystals with a melting temperature T_m of 51−52 °C formed by side-by-side packed octadecyl (C18) side chains are responsible for more than 99% of effective cross-links in c-IPNs, the rest being hydrophobic associations and chemical cross-links. The c-IPNs exhibit varying stiffness (9−34 MPa), stretchability (72−740%), and a significantly higher toughness (1.9−12 MJ·m^{-3}) than their components, which can be tuned by changing the IIR/PC18A weight ratio. The properties of c-IPNs could also be tuned by incorporating a second, noncrystallizable hydrophobic monomer, namely, lauryl methacrylate (C12M), in the melt mixture. We show that the lamellar clusters acting as sacrificial bonds break at the yield point by dissipation of energy, while the ductile amorphous continuous phase keeps the structure together, leading to the toughness improvement of c-IPNs. They exhibit a two-step healing process with >90% healing efficiency with respect to the modulus and a complete shape-recovery ratio induced by heating above T_m of alkyl crystals. The temperature-induced healing occurs via a quick step where C18 bridges form between the damaged surfaces followed by a slow step controlled by the interdiffusion of C18A segments in the bulk. We also show that the strategy developed here is suitable for a variety of rubbers and *n*-alkyl (meth)acrylates of various side-chain lengths.

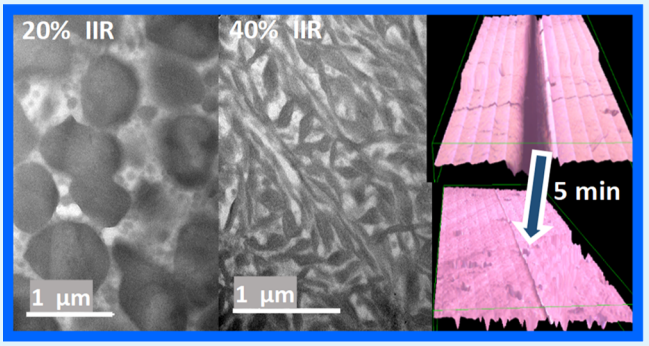

KEYWORDS: *butyl rubber, n-octadecyl acrylate, interconnected IPNs, self-healing, shape memory*

1. INTRODUCTION

Preparation of self-healing elastomers without compromising their mechanical performance attracts significant interest in recent years to enable them a long service life and hence to reduce the environmental issues.[1] In addition to self-healing, shape memory in elastomers is an important property for applications in implants for minimally invasive surgery, actuators, and sensors.[2] Several studies have been conducted to prepare supramolecular self-healable elastomers via various intermolecular interactions.[3−12] For instance, interpenetrating polymer network (IPN) elastomers with self-healing and/or shape-memory functions have recently been reported that consist of elastomeric and semicrystalline poly(ε-caprolactone) components.[13,14] However, a more promising approach would be to generate self-healing in commercially available and widely used rubbers. For this purpose, sulfur vulcanization of rubbers was conducted in the presence of additives such as copper catalysts triggering self-healing[15,16] or by increasing the amount of reversible disulfide bonds in vulcanized rubber.[17,18] Alternatively, reversible cross-links were introduced into commercial rubbers via molecular diffusion,[19,20] reversible covalent bonds,[21−26] noncovalent interactions such as hydrogen bonding,[1,27,28] and ionic interactions.[29−34] However, most of the techniques reported so far to create self-healing require chemical modification of commercial rubbers, whereas those making use of the unmodified rubbers result in a low healing efficiency or a low mechanical strength. Alternatively, blends based on various rubbers have also been designed to generate

Received: February 27, 2021
Accepted: April 16, 2021
Published: April 28, 2021

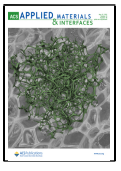

https://doi.org/10.1021/acsami.1c03814
ACS Appl. Mater. Interfaces 2021, 13, 21786−21799

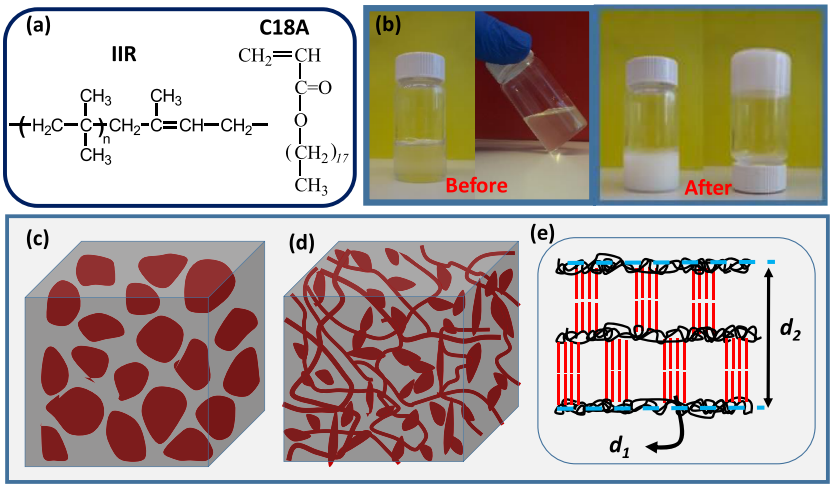

Figure 1. (a) Structure of IIR (n = 58) and the C18A monomer. (b) Images of an IIR/C18A/Irgacure mixture at 30 ± 2 °C before (left) and after UV polymerization (right). IIR = 30 wt %. (c,d) Schemes showing sea-island (c) and co-continuous morphologies (d) of IIR/PC18A c-IPNs. The amorphous interpenetrating IIR and PC18A networks interlinked via C18A segments are shown in gray, while the crystalline domains are shown in dark red. (e) Scheme showing lamellar crystals of c-IPNs. Crystallized side chains and amorphous layers are shown in red and black, respectively.

self-healing and shape-memory functions.[35−41] Brostowitz et al. prepared a shape-memory polymer by swelling cross-linked natural rubber with stearic acid at 75 °C followed by cooling to form crystalline platelets fixing the temporary shape of the rubber.[42]

Flexible polymers with long alkyl side chains such as poly(*n*-alkyl acrylate)s are known to arrange themselves into crystalline structures.[43] The crystallization of the side chains independent of the polymer backbone provides the side-chain length of poly(*n*-alkyl acrylate)s as a tunable parameter to control their physical properties such as the melting temperature, size of alkyl crystals, and gas permeability.[44−48] Side-chain crystalline polymers in bulk, solution, and gel states emphasize the importance of the cooperative hydrophobic interactions among the alkyl side chains.[43,49−55] Self-organization of the side chains into lamellar crystals is associated with the partial alignment of the polymer backbone, which requires flexible hydrophilic backbones having alkyl side chains longer than 16 carbon atoms. The thermally tunable physical properties of poly(*n*-alkyl acrylate)s attract interest for many applications including shape-memory materials,[55−57] pressure-sensitive adhesives,[58] and smart membranes.[47]

One drawback of long side-chain poly(*n*-alkyl acrylate)s is that they are brittle in tension due to the lack of an efficient energy dissipation mechanism. Here, we describe, for the first time to our knowledge, a simple and versatile strategy for the preparation of highly tough and highly stretchable interconnected IPNs (c-IPNs) based on butyl rubber (IIR) and poly(*n*-octadecyl acrylate) (PC18A). They were prepared by solvent-free UV polymerization of *n*-octadecyl acrylate (C18A) at 30 ± 2 °C in the presence of IIR (Figure 1a). IIR, a copolymer of isobutylene with a small amount of isoprene units (0.5−4 mol %), is an amorphous synthetic elastomer with many attractive properties such as high gas and water impermeability and biocompatibility. Sulfur vulcanization of IIR through its unsaturated isoprene units improves its mechanical properties and abrasion resistance and provides a wide range of applications.[59−61] IIR without chemical modification has not been used before as the starting material for self-healing studies likely because of its low unsaturation degree requiring powerful accelerators for its vulcanization than the other rubbers.

Our preliminary experiments showed that IIR is easily soluble in the hydrophobic C18A monomer above its melting temperature T_m, 30 °C (Figure 1b). This provides solvent-free photopolymerization of C18A in the presence of IIR and a UV initiator, 2-hydroxy-4′-(2-hydroxyethoxy)-2-methylpropiophenone (Irgacure 2959). Melt mixing of the reaction components followed by UV polymerization at 30 ± 2 °C leads to IIR/PC18A c-IPNs with sea-island or co-continuous morphologies depending on their IIR contents (Figure 1c,d). The lamellar crystals formed by side-by-side packed octadecyl (C18) side chains are responsible for more than 99% of effective cross-links in c-IPNs, the rest being hydrophobic associations and chemical cross-links. They exhibit varying stiffness (9−34 MPa), stretchability (72−740%), and a significantly higher toughness (1.9−12 MJ·m^{-3}) than their components, which can be tuned by changing the IIR/C18A weight ratio in the melt mixture. The properties of c-IPNs could also be tuned by incorporating a second, noncrystallizable hydrophobic monomer, namely, lauryl methacrylate (C12M) in the melt mixture. We show that the lamellar clusters acting as sacrificial bonds break at the yield point by dissipation of energy, while the ductile amorphous continuous phase keeps the structure together, leading to the toughness improvement of c-IPNs. They exhibit a two-step healing process with >90% healing efficiency with respect to the modulus and a complete shape-recovery ratio induced by heating above T_m (51−52 °C) of alkyl crystals. We also show that the strategy developed here is suitable for a variety of rubbers and n-alkyl (meth)acrylates of various side-chain lengths.

2. RESULTS AND DISCUSSION

2.1. Material Preparation. c-IPNs based on IIR and PC18A were prepared by melt-mixing of the reaction components IIR rubber, C18A monomer, and Irgacure 2959 photoinitiator followed by the in situ polymerization of C18A under UV light at 360 nm. The onset of melting and melting temperatures of the C18A monomer are 28 and 30 °C, respectively, while incorporation of IIR slightly reduced these temperatures (Figure S1). Thus, dissolving IIR in the C18A

https://doi.org/10.1021/acsami.1c03814
ACS Appl. Mater. Interfaces 2021, 13, 21786−21799

melt at 80 °C followed by cooling to 30 °C resulted in a transparent IIR-C18A mixture (Figure 1b). The IIR content of the mixture could be increased up to 40 wt % because at higher rubber concentrations, it was too viscous to ensure homogeneity (Figure S2). After running the polymerization for 1 h at 30 ± 2 °C under UV light, IIR/PC18A c-IPNs were obtained that were opaque in appearance, reflecting the existence of submicron-sized domains (Figure 1b, see also Supporting Information Text T1 and Figure S3). This is expected due to the incompatibility of IIR and PC18A components having the solubility parameters 16.8 and 17.7 $(MPa)^{0.5}$, respectively.[60,62] Table 1 shows the composition,

Table 1. Melting (T_m) and Crystallization Temperatures (T_{cry}), Crystallinity Fraction f_{cry}, and Tensile Mechanical Properties of IIR/PC18A c-IPNs[a]

IIR/C18A by weight	T_m/°C	T_{cry}/°C	f_{cry}	E/MPa	W/MJ·m^{-3}	ε_f %
0/100	54.5 (0.3)	38.0 (0.2)	0.50	42 (3)	0.37 (0.05)	18 (3)
20/80	51 (2)	38.8 (0.1)	0.24	34 (2)	1.9 (0.1)	72 (6)
30/70	52.0 (0.4)	40.0 (0.1)	0.20	11.1 (0.1)	6.9 (0.7)	360 (31)
40/60	52 (2)	40.6 (0.1)	0.14	9 (1)	12 (1)	740 (66)
100/0			0	0.6	1.3 (0.1)	760 (62)

[a] E = Young's modulus. W = toughness (the area under the stress–strain curve). ε_f = elongation at break. The properties of IIR/PC18A-C12M c-IPNs are shown in Table S1. Standard deviations are given in parentheses. For f_{cry}, they are smaller than 5%. Each T_{cry} or T_m value is the average of at least three measurements conducted on different samples from each group.

melting, and crystallization temperatures, the crystallinity fraction, and tensile mechanical properties of IIR/PC18A c-IPNs together with the neat IIR and PC18A prepared under the same experimental condition but in the absence of IIR. In the following paragraphs, c-IPNs are denoted by the weight percent of IIR in IIR/C18A mixtures. Thus, a c-IPN with 40 wt % IIR means that the melt mixture is composed of 40 wt % IIR and 60 wt % C18A.

2.2. Microstructure and Morphology. c-IPNs were insoluble in toluene (extractable less than 5 wt %), a good solvent for both IIR and PC18A, indicating the occurrence of the cross-linking reactions between the unsaturated isoprene units of IIR and the growing PC18A radicals. Their FTIR spectra present characteristic peaks of PC18A and IIR at 1730 and 1366 cm^{-1}, respectively, corresponding to the stretching vibration of C=O in PC18A and bending vibration of CH_3 in IIR (Figure S4). Increasing IIR content of c-IPN also increases the peak intensity at 1366 cm^{-1}, while that at 1730 cm^{-1} decreases. Figure 2a,b shows XRD and SAXS patterns of IIR/PC18A c-IPNs, respectively, with various IIR contents. XRD patterns exhibit a broad diffusion peak at 14.5° which is typical for amorphous IIR[63] and a small diffraction peak at ~5.2° which is due to the partially crystallized side-chain domains with a *Bragg d*-spacing of ~1.6 nm.[53,64] The main sharp peak appears at 21.4° corresponding to a d_1-spacing of 0.41 nm. This spacing is typical for side-by-side packed paraffin-like alkyl chains[43,45−53] and reflects the distance between two octadecyl side chains along the same backbone (Figure 1e). SAXS data in Figure 2b provide insights about how the thickness of these

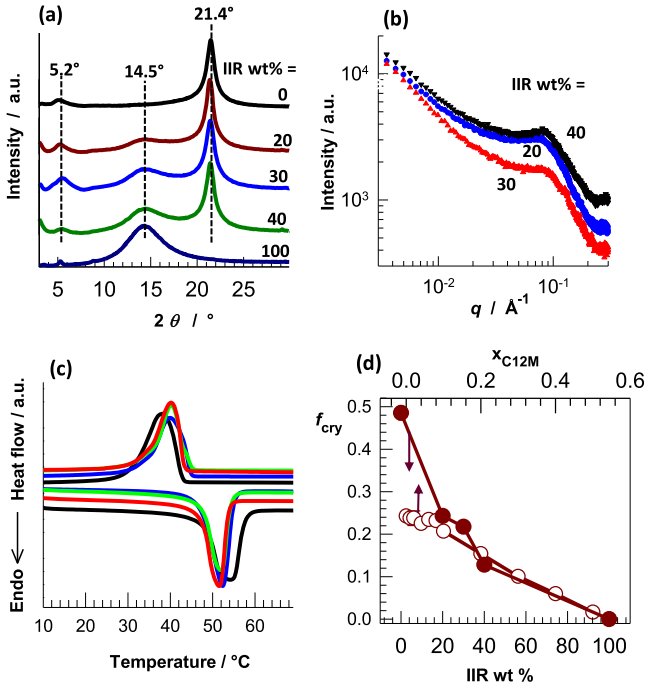

Figure 2. (a–c) XRD (a), SAXS (b), and DSC patterns (c) of c-IPNs with various IIR contents. In (c), IIR = 0 (black), 20 (red), 30 (blue), and 40 wt % (green). (d) Degree of crystallinity f_{cry} plotted against IIR wt % (filled symbols) and x_{C12M} (open symbols). Error bars are smaller than the size of the symbols.

crystals changes with the rubber content. The sample with 40 wt % IIR exhibits a broad peak at 0.08 Å^{-1} corresponding to a d_2-spacing of 7.9 nm. This spacing is attributed to the distance between two tightly packed side chains, that is, backbone-to-backbone distance. It is larger than twice the fully extended octadecyl chain (2 × 2.43 nm) due to the thickness of the amorphous polymer backbone and noncrystallized methylene units of the octadecyl chain (Figure 1e). The intensity of this peak decreases and becomes broader in the order 40 > 20 > 30 wt % IIR. For pure PC18A or copolymers of C18A, this peak is much sharper and d_2 spacing is around 6 and 5 nm for their wet and dry states, respectively.[45,49,54] The broadness of the peak in IIR/PC18A as compared to PC18A reveals that their crystalline phase is not a well-ordered state, likely due to the confinement of octadecyl side chains within the amorphous polymer, restricting their alignment to form alkyl crystals.

Figure 2c shows DSC scans of c-IPNs with various IIR contents together with the pure PC18A. DSC analysis shows melting T_m and recrystallization peaks T_{crys} at 51–52 and 39–41 °C, respectively, independent of the IIR content (Table 1). The degree of crystallinity f_{cry}, that is, the mole fraction of C18A units involved in crystalline domains, decreases from 24 to 14% with increasing IIR content from 20 to 40 wt % (filled symbols in Figure 2d). These f_{cry} values are much lower than that of pure PC18A (50%) due to the presence of amorphous IIR chains, restricting the alignment of PC18A backbones. The degree of crystallinity f_{cry} could also be adjusted at a fixed IIR content by replacing part of C18A units with lauryl methacrylate (C12M) ones, which are noncrystallizable.[65] The open symbols in Figure 2d represent f_{cry} of IIR/PC18A-C12M c-IPNs composed of 20 wt % IIR with the rest being the mixed hydrophobes (C18A + C12M) plotted against the mole fraction of C12M, x_{C12M}. Increasing x_{C12M} decreases both the

https://doi.org/10.1021/acsami.1c03814
ACS Appl. Mater. Interfaces 2021, 13, 21786−21799

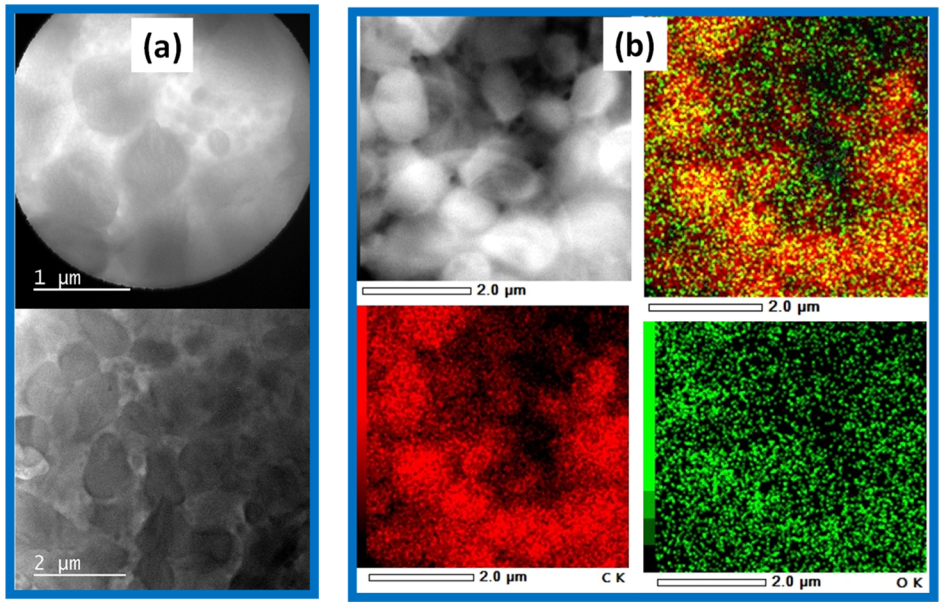

Figure 3. (a) TEM images of an unstained IIR/PC18A sample with 20 wt % IIR at two different magnifications in the BF mode. Scale bars: 1 (up) and 2 μm (down). (b) STEM image of the same sample in the DF mode and its EDX maps. The elemental distributions for C and O in EDX maps are shown in red and green, respectively, while overlapping red and green signals appear yellow. Scale bars: 2 μm.

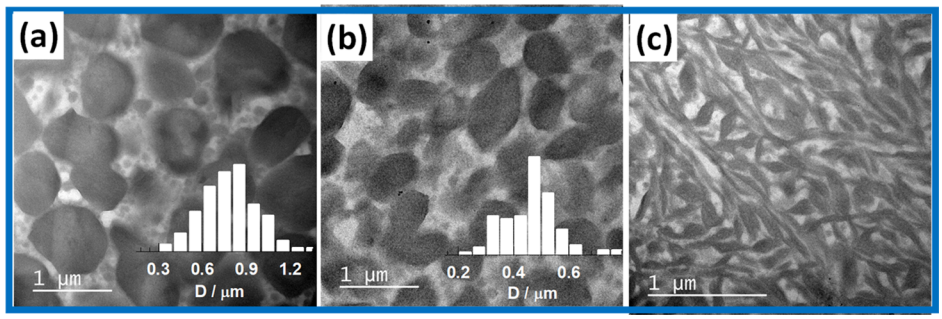

Figure 4. TEM images of UranyLess-stained c-IPNs with 20 (a), 30 (b), and 40 wt % IIR (c), while the insets of (a) and (b) show the size distribution of the particles. Scale bars: 1 μm.

degree of crystallinity and the melting temperature of the c-IPNs, indicating decreasing stability of alkyl crystals (Table S1 and Figure S5).

Figure 3a presents the morphology of an unstained IIR/PC18A sample with 20 wt % IIR at two different magnifications observed by transmission electron microscopy (TEM) in the bright-field (BF) mode. Since the sample is unstained, the contrast observed has a structural origin. A small objective aperture is used in the upper image for contrast enhancement between the amorphous and crystalline domains. The crystalline areas forming the particles in the sample appear dark, and the amorphous ones appear bright. Because IIR and PC18A components of c-IPNs have the repeating units C_4H_8 and $C_{21}H_{40}O_2$, respectively, the spatial distribution of PC18A domains in the sample can be identified by elemental oxygen mapping. Figure 3b shows a dark-field (DF) scanning TEM (STEM) image of an unstained sample with 20 wt % IIR and its energy-dispersive X-ray spectroscopy (EDX) maps. The STEM image highlights the crystalline domains, forming the particles as bright areas due to the DF mode. In the EDX maps, the elemental distributions for C and O are shown in red and green, respectively, while overlapping red and green signals, that is, C and O atoms, appear yellow. Although localization of C and O atoms is seen in the particles, they also distribute over the whole investigated area. The single-point STEM−EDX measurements across the STEM image in Figure 3b indeed reveal a higher O content within the particles as compared to the outer continuous phase. From these findings, we can conclude that the crystalline domains composed of lamellar crystals and interconnected amorphous PC18A and IIR chains bridging the crystals form the dispersed phase, while the noncrystalline interpenetrating PC18A and IIR form the continuous phase of the c-IPNs, as schematically presented in Figure 1c.

Figure 4a−c presents TEM images of UranyLess-stained c-IPN samples containing 20, 30, and 40 wt % IIR, respectively, and the insets to a and b show the size distribution of the particles. The samples with 20 and 30 wt % IIR exhibit a sea-island morphology with crystalline domains dispersed in the continuous amorphous matrix. Increasing IIR content from 20 to 30 wt % decreases the number-average particle size d_n from 800 to 468 nm at a polydispersity index of 1.07. When IIR content is further increased to 40 wt %, a shift from sea-island to co-continuous morphology appears. This change in the morphology can be explained with the viscosity of the IIR/C18A mixture at 30 °C before the photopolymerization

https://doi.org/10.1021/acsami.1c03814
ACS Appl. Mater. Interfaces 2021, 13, 21786−21799

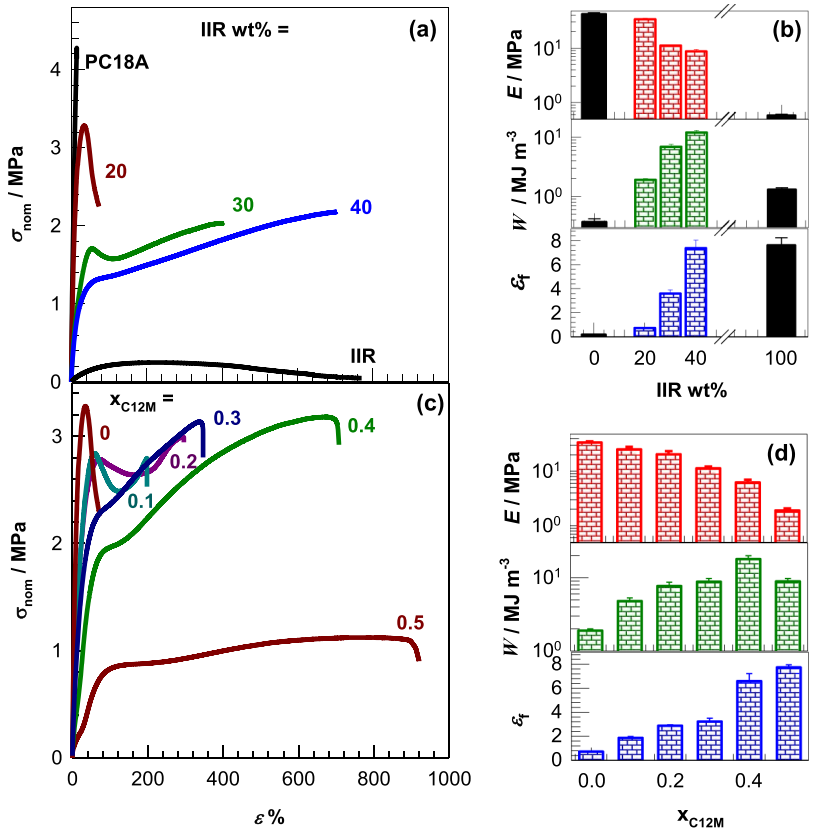

Figure 5. (a,b) Stress−strain curves (a) and the mechanical parameters (b) of IIR/PC18A c-IPNs prepared at various IIR wt %. E = Young's modulus, W = toughness, and ε_f = elongation at break. (c,d) Same plots as in the top panel but for IIR/PC18A-C12M c-IPNs at various x_{C12M}. IIR = 20 wt %. Note that the last point on each stress−strain curve corresponds to the breaking point, that is, the stress of the next data point is zero.

(Figure S2). The zero-shear viscosity of the mixture drastically increases from 84 to 1540 Pa·s with increasing IIR content from 20 to 40 wt %. Thus, at a low viscosity, the growing PC18A radical chains during polymerization will push apart the pre-existing, flexible IIR chains so that a phase-separated c-IPN with sea-island morphology is obtained.[66] As the viscosity increases, the diffusion of the growing PC18A radicals will be restricted and agglomeration between the particles is hindered, leading to a decrease in the particle size. At the highest viscosity, that is, at 40 wt % IIR, the positions of IIR chains will hardly be changed so that the growing PC18A radicals can diffuse through the nanochannels of the pre-existing IIR physical network to form a co-continuous morphology.

2.3. Mechanical and Viscoelastic Properties. In Figure 5a,b, the stress−strain curves (a) and mechanical parameters (b) of IIR/PC18A c-IPNs are compared with those of the neat IIR and PC18A presented by black curves and bars, respectively. Young's modulus E and the elongation at break ε_f of IIR and PC18A components represent two extremes, while those of the c-IPNs could be tuned between them by changing the composition of the melt mixture. With increasing IIR content from 20 to 40 wt %, that is, with decreasing degree of crystallinity, E decreases from 34 to 9 MPa, while the elongation at break ε_f increases from 72 to 740% (Table 1). Moreover, they exhibit yielding-type behavior with a yield stress increasing with the degree of crystallinity and finally becomes the fracture point of PC18A (Figure 5a). The toughness W (the area under the stress−strain curve) of c-IPNs increases from 1.9 to 12 MJ·m^{-3} as the IIR content is increased (Table 1). Particularly remarkable is that all c-IPNs exhibit a higher toughness than their components (Figure 5b). For instance, the c-IPN with 40 wt % IIR exhibits 10- and 33-fold higher toughness as compared to the neat IIR and PC18A, respectively, without affecting the high stretchability of IIR (∼700%).

Besides the IIR content, mechanical properties of the c-IPNs can also be tuned by replacing part of C18A units with the weak hydrophobe C12M, which is unable to form crystalline domains. Figure 5c,d presents stress−strain curves and mechanical parameters of IIR/PC18A-C12M c-IPNs prepared at 20 wt % IIR with the rest being C18A + C12M at various C12M mole fractions (x_{C12M}). The toughness of IIR/PC18A without C12M, denoted by 0, significantly increases after incorporation of the noncrystallizable C12M segments into the polymer (Table S1). At x_{C12M} = 0.40, IIR/PC18A-C12M exhibits a toughness of 18 MJ·m^{-3} and Young's modulus of 6.2 MPa and sustains 660% elongation under 2.9 MPa stress.

The appearance of yielding behavior and significant toughness improvement of c-IPNs with increasing IIR content or upon incorporation of the weak hydrophobe C12M into PC18A is attributed to the increasing amount of the amorphous polymers bridging the lamellar crystals. The interlamellar amorphous polymers that are able to unfold under an external force, that is, so-called tie molecules, are known to play a significant role in the mechanical strength and yield the behavior of semicrystalline polymers and hydrogels.[67−72] The crystalline domains in the dispersed or co-continuous phases of IIR/PC18A are composed of lamellar crystals separated by amorphous interlamellar layers (Scheme S1a). Upon application of an external force, amorphous layers

https://doi.org/10.1021/acsami.1c03814
ACS Appl. Mater. Interfaces 2021, 13, 21786−21799

between the crystals unfold to form active tie molecules interconnecting lamellar clusters consisting of stacks of lamellar crystals (Scheme S1b).[69−71] The active tie molecules are responsible for energy dissipation by transmitting the external force between the lamellar clusters during which the clusters are deformed and finally fragmented at the yield point. The yield stress σ_y of semicrystalline polymers at which the lamellar clusters start to disintegrate into their fragments is given by the lamellar crystal model as[69−71]

$$\sigma_y = 2\sqrt{2EU_y}\,(L/l)^2 \tag{1}$$

where U_y is the yield energy, that is, the area under the stress−strain curve up to the yield point, L represents the lamellar cluster thickness, and l is the spacing between tie molecules bridging these clusters ($l > L$). Figure 6a showing the σ_y versus

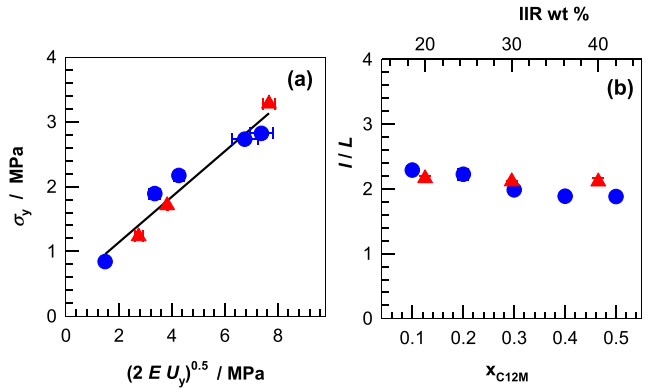

Figure 6. (a) Yield stress σ_y vs $\sqrt{2EU_y}$ plot for c-IPNs with various IIR (red triangles) and C12M contents (blue circles). (b) l/L ratio shown as a function of IIR (triangles) and C12M contents (circles).

$\sqrt{2EU_y}$ plot for c-IPNs with various IIR and C12M contents reveals that all the data fall on the same line with a slope of 0.43 ± 0.02 corresponding to l/L = 2.1 ± 0.1 (Figure 6b). A l/L value of around 2 has already been reported for semicrystalline polyethylene and isotactic polypropylene[68,70,71] and semicrystalline hydrogels[72] and indicates that the minimum spatial dimension of the fragmented lamellar clusters is equal to that of a single chain.[69−71] The yielding behavior of IIR/PC18A c-IPNs with or without C12M can thus be explained with the breakup of lamellar clusters at the point of yield. The clusters acting as sacrificial bonds break at the yield point by dissipation of energy, while the ductile amorphous continuous phase keeps the sample together, leading to the toughness improvement of c-IPNs.

The crystalline domains in c-IPNs acting as physical cross-links provided a drastic change in their mechanical properties depending on the temperature. To highlight this feature, temperature sweeps between below and above T_m of the c-IPNs were conducted using a parallel-plate rheometer. Figure 7a shows the storage modulus G' of IIR/PC18A with various IIR contents during a cooling/heating cycle between 65 and 25 °C. G' reversibly varies by around 3 orders of magnitude with a change in temperature between below and above T_m or T_{crys}, as indicated by the dashed vertical lines. For example, G' of the sample with 20 wt % IIR is 10.300 and 9 kPa at 25 and 65 °C, respectively, that is, it 1140-fold reversibly changes depending on the temperature. The higher the IIR content, the higher is G' at above T_m due to the simultaneous increase in the viscosity of the melt mixture (Figure S2), while an opposite behavior appears below T_m because of the decreasing degree of crystallinity (Table 1).

Similar temperature responses were also observed in IIR/PC18A-C12M with various C12M contents (Figure S6); increasing C12M mole fraction x_{C12M}, that is, decreasing crystallinity, also decreases the magnitude of modulus change between below and above T_m. Figure 7b,c shows frequency dependences of G' and the loss factor tan δ (= G'/G' where G'' is the loss modulus) of IIR/PC18A at 25 and 65 °C, respectively. At 25 °C, G' is independent of the frequency, while at 65 °C, it exhibits a power law behavior with an exponent 0.14 ± 0.01, revealing their viscoelastic nature. The fact that tan δ remains below unity after melting of the alkyl crystals indicates the existence of chemical cross-links and hydrophobic associations, keeping the 3D network structure stable in the melt state.

2.4. Type of Intermolecular Cross-Links. The results reveal that the c-IPNs contain alkyl crystals and associations of alkyl side chains serving as strong and weak physical cross-links, respectively. In addition, their insolubility in a good solvent also indicates the presence of chemical cross-links between the unsaturated isoprene units of IIR and PC18A. One may ask how each of these cross-links contributes to the total cross-link density of c-IPNs. Assuming additivity of the cross-links, the cross-link density ν_e of IIR/PC18A is presented by

$$\nu_e = \nu_{e,cry} + \nu_{e,assoc} + \nu_{e,chem} \tag{2}$$

where $\nu_{e,cry}$, $\nu_{e,assoc}$, and $\nu_{e,chem}$ are the contributions of alkyl crystals, hydrophobic associations, and chemical cross-links, respectively. To estimate the relative contribution of elastically effective intermolecular bonds to the cross-link density ν_e, we used the storage moduli of IIR/PC18A measured at 25 and 65 °C, $G'_{25°C}$ and $G'_{65°C}$, at which they are in semicrystalline and amorphous states, respectively. Assuming that G' at 6.32 rad·s^{-1} (1 Hz) is equal to the shear modulus G and the network chains deform affinely, the cross-link density can be estimated by[73−75]

$$\nu_e = \frac{G'_{25°C}}{RT} \tag{3}$$

$$\nu_{e,assoc} + \nu_{e,chem} = \frac{G'_{65°C}}{RT} \tag{4}$$

where R is the gas constant and T is the absolute temperature. Moreover, because the crystalline domains and hydrophobic associations completely dissociate in good solvents such as toluene,[49,50,54,76] it is likely that the swollen c-IPNs containing around 95% toluene only have chemical cross-links. The density of chemical cross-links $\nu_{e,chem}$ was estimated from both the equilibrium swelling ratio q_w and Young's modulus E (=3G) of the swollen c-IPNs using the equations[74]

$$\nu_{e,chem} = \frac{-[\ln(1-\phi_2) + \phi_2 + \chi(\phi_2)^2]}{V_1(\phi_2^{1/3} - \phi_2/2)} \tag{5a}$$

$$\nu_{e,chem} = \frac{E}{3RT(\phi_2)^{1/3}} \tag{5b}$$

where ϕ_2 is the volume fraction of IIR/PC18A in its equilibrium swollen state in toluene, χ is the polymer−solvent interaction parameter, given by χ = 0.49 + 0.25 ϕ_2 for the IIR-

https://doi.org/10.1021/acsami.1c03814
ACS Appl. Mater. Interfaces 2021, 13, 21786−21799

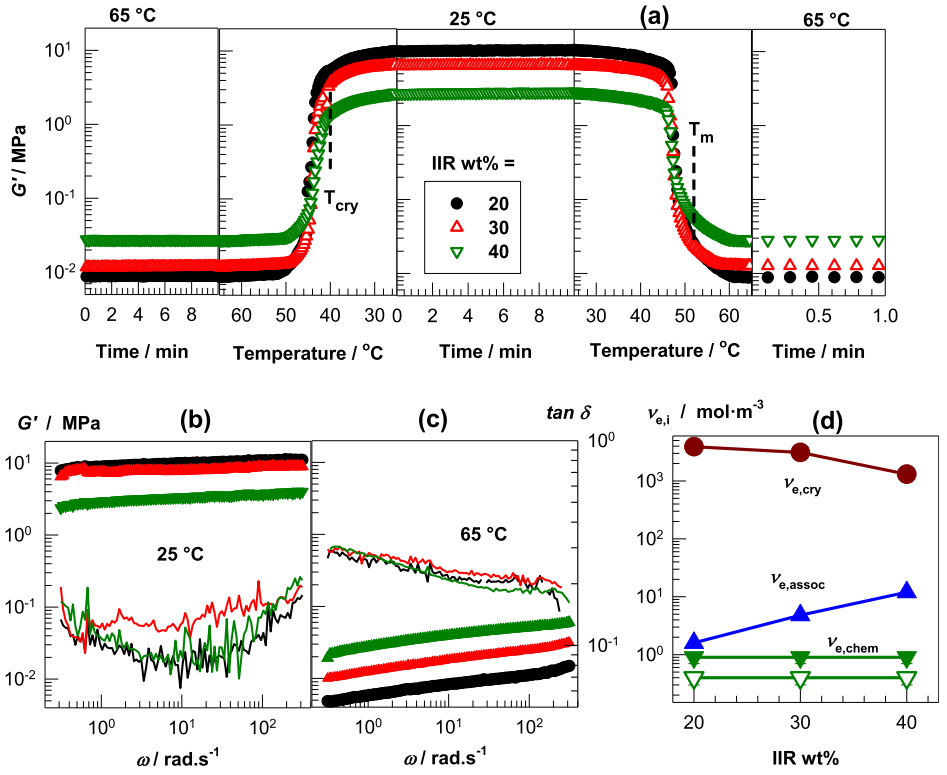

Figure 7. (a) Variation of G' of IIR/PC18A with various IIR contents during a thermal cycle between 65 and 25 °C. ω = 6.3 rad·s^{-1}. γ_o = 0.1%. T_m and T_{crys} are indicated by the dashed vertical lines. (b,c) Frequency (ω) dependences of G' (symbols) and tan δ (curves) of IIR/PC18A at 25 (b) and 65 °C (c). γ_o = 0.1% IIR = 20 (circle), 30 (triangle up), and 40 wt % (triangle down). (d) Components $\nu_{e,cry}$, $\nu_{e,assoc}$, and $\nu_{e,chem}$ of the cross-link density of c-IPNs shown as a function of IIR wt %. The filled and open down-triangles represent $\nu_{e,chem}$ values estimated using eqs 5aa and 5b, respectively.

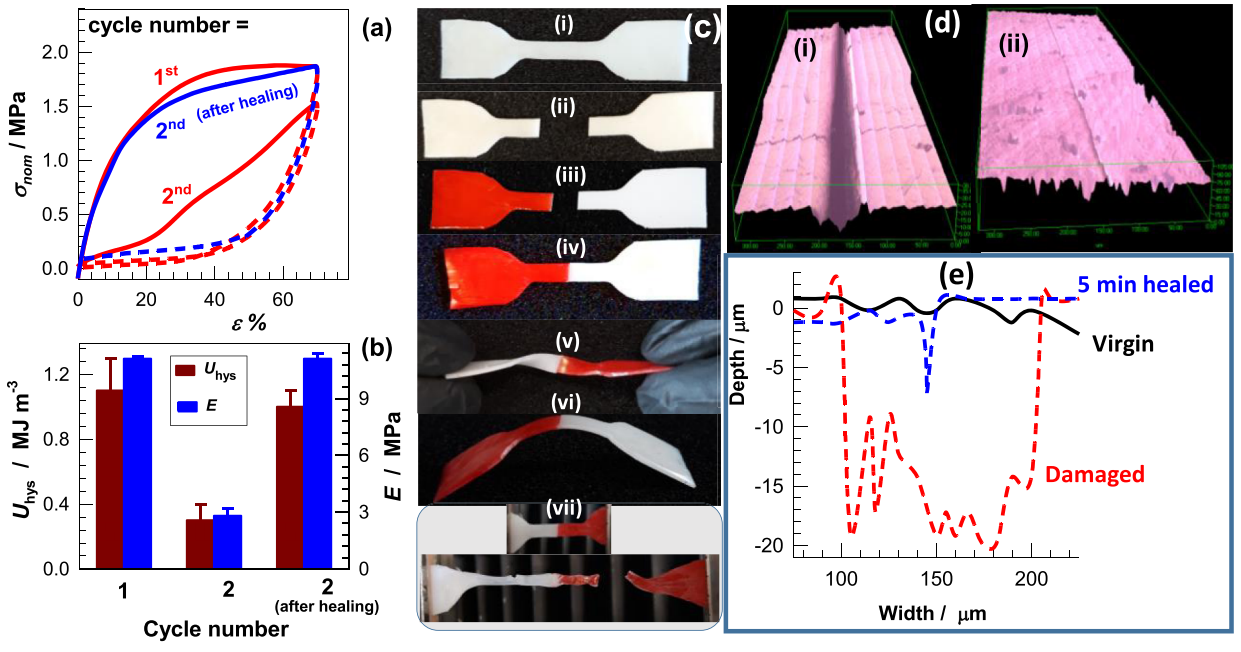

Figure 8. (a) Two successive tensile loading (solid curves) and unloading cycles (dashed curves) without a waiting time between cycles up to a maximum strain (ε_{max}) of 70%. The second loading was conducted before (red) and after healing (blue). IIR = 30 wt %. γ = 5 min^{-1}. (b) U_{hys} and E of IIR/PC18A c-IPN with 30 wt % IIR calculated from the first and second mechanical cycles before and after healing. (c) Images of an IIR/PC18A specimen with 30 wt % IIR before (i) and after cutting (ii), after coloring one of its parts with a dye for clarity (iii), and after healing at 65 °C for 1 h (iv). The healed specimen can be twisted (v), bended (vi), and stretched to a stretch ratio of 320 ± 10% (vii), which is 88 ± 3% of the virgin sample. (d) Images of the same specimen after creating a cut of around 20 μm in depth and 100 μm in width (i) and after healing at 65 °C for 5 min (ii). (e) Depth and width profiles of the same specimen before and after cutting and after healing for 5 min.

https://doi.org/10.1021/acsami.1c03814
ACS Appl. Mater. Interfaces 2021, 13, 21786−21799

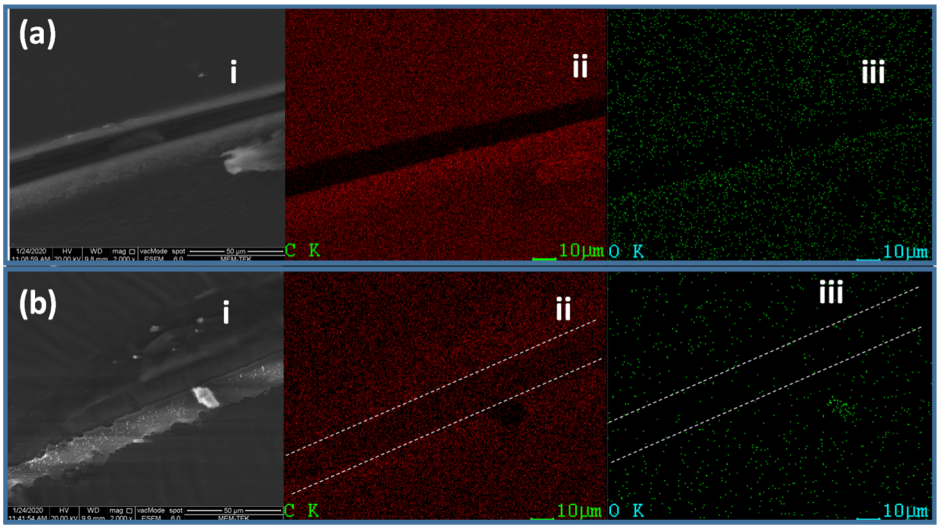

Figure 9. SEM images (i) and elemental mapping of C (ii) and O atoms (iii) for IIR/PC18A with 40 wt % IIR after cutting (a) and after healing at 50 °C for 5 min (b). The parallel white lines in the bottom panel surround the healed area.

toluene system in the range of ϕ_2 between 0.01 and 0.10,[77] and V_1 is the molar volume of toluene (106 mL·mol^{-1}). The volume fraction ϕ_2 was calculated from the equilibrium weight swelling ratio q_w using $\phi_2 = d_1/(\rho q_w)$ where ρ are d_1 are the densities of IIR (0.92 g·mL^{-1})[77] and toluene (0.867 g·mL^{-1}), respectively. IIR/PC18A c-IPNs exhibit a swelling ratio q_w of 20 ± 3 in toluene and a Young's modulus E of 3.1 ± 0.4 kPa at 23 ± 2 °C in their equilibrium swollen states in toluene. Using these values, $\nu_{e,chem}$ was estimated as 0.9 ± 0.2 and 0.4 ± 0.1 mol·m^{-3} using eqs 5a and 5b, respectively. Figure 7d shows $\nu_{e,cry}$, $\nu_{e,assoc}$, and $\nu_{e,chem}$ calculated using eqs 2−5a plotted against IIR content of c-IPNs. The chemical cross-link density $\nu_{e,chem}$ is very small and only contributes to less than 0.1% of the total cross-link density of c-IPNs, as expected from their high swelling degrees in toluene. The main component determining ν_e is the alkyl crystals forming 99.0−99.9% of the total effective cross-link density. Increasing IIR content of c-IPNs also increases the number of effective cross-links due to the hydrophobic association ($\nu_{e,assoc}$), and at 40 wt % IIR, $\nu_{e,assoc}$ contributes to around 1% of the total cross-links.

2.5. Self-Healing and Shape-Memory Behavior. As would be expected from the physical nature of more than 99% cross-links, all c-IPNs with or without C12M exhibited healing behavior when heated above T_m of crystalline domains and subsequently cooled to room temperature. We first utilized cyclic mechanical tests to demonstrate self-recoverability of IIR/PC18A c-IPNs. Five successive tensile loading and unloading cycles of IIR/PC18A conducted for a maximum strain ε_{max} of 70% without a resting period between cycles showed a significant mechanical hysteresis during the first cycle (Figure S7). This reflects irreversible breaking of the alkyl crystals that mainly contribute to the cross-link density of c-IPNs. For instance, the solid and dashed red curves in Figure 8a show two successive loading and unloading curves, respectively, up to ε_{max} = 70% for a sample with 30 wt % IIR. The modulus E and the hysteresis energy U_{hys} (the area surrounded by the loading and unloading curves) of the virgin specimen drastically decrease from 11.1 to 2.8 MPa and from 1.1 to 0.3 MJ·m^{-3}, respectively, after the first cycle, revealing the occurrence of a permanent damage that cannot be healed autonomously (Figure 8b). However, when the internally damaged sample after the first cycle is heated at 50 °C for 15 min and subsequently cooled to 23 ± 2 °C, the second loading curve closely follows the first one, indicating heating-induced recovery of the virgin microstructure (solid blue curve in Figure 8a). Both the hysteresis energy U_{hys} and the modulus E could completely be recovered after the heating-cooling treatment of the sample (Figure 8b).

To demonstrate macroscopic healing behavior of IIR/PC18A, the specimens were first cut into two halves and then put in contact at 65 °C several times. Figure 8c shows the images of an IIR/PC18A specimen with 30 wt % IIR before (i) and after cutting (ii), after coloring one of the cut parts with a dye for clarity (iii), and after 1 h healing time at 65 °C (iv). The healed specimen can be twisted (v), bended (vi), and stretched to a stretch ratio of 320 ± 10% (vii), which is 88 ± 3% of the virgin sample. To monitor the time-dependent healing behavior, a cut of 73 μm in diameter was first created on a cylindrical specimen using a blade. After heating the specimen at 65 °C and then cooling to 23 ± 2 °C, the change in the cut diameter was monitored as a function of the heating time under an optical microscope. Within the first hour, the large cut disappeared to form several small cuts at the surface, while at longer times, the cut regions slowly decreased in size becoming 6−14 μm after 24 h (Figure S8). This two-step healing process was also observed by confocal microscopy measurements. Figure 8d shows typical images of an IIR/PC18A sample with 30 wt % IIR after creating a cut of around 20 μm in depth and 100 μm in width (i) and after healing at 65 °C for 5 min (ii). The surface roughness (R_a) of the virgin sample is 0.94 μm, and it increases to 1.28 μm after cutting, whereas it returns to a value of 1.07 μm after 5 min of healing. The depth and width profiles of the sample shown in Figure 8e reveal a significant healing within 5 min. Healing efficiency along the width of the damaged area was 76% after a healing time of 5 min.

The rapid healing within 5 min and the chemical composition of the cut region before and after healing were monitored by SEM−EDX measurements. Figure 9a,b shows SEM images (i) and elemental mapping of C (ii) and O atoms (iii) for an IIR/PC18A specimen with 40 wt % IIR. In accordance with the real atomic composition of oxygen in the

https://doi.org/10.1021/acsami.1c03814
ACS Appl. Mater. Interfaces 2021, 13, 21786−21799

c-IPNs, oxygen composition obtained from EDX analysis decreases from around 8 to 6 wt % with increasing IIR content from 20 to 40 wt %, revealing reliability of the EDX data (Figure S9). EDX images were taken after cutting (a, upper panel) and after healing at 50 °C for 5 min (b, bottom panel). It is seen that the thickness of the cut decreases from around 15 to 2 μm within 5 min. Moreover, the spatial distributions of C and O atoms in the healed region (the area surrounded by the white dotted lines in Figures 9b and S10) reveal that this region is rich in carbon atoms, that is, the fast healing process occurs via filling of that area with alkyl chains.

The two-step healing of the c-IPNs can be explained with the existence of fast and slow processes occurring on the cut surfaces and in the bulk region, respectively. The surfaces of poly(alkyl (meth)acrylate)s in contact with air are known to be covered by the alkyl side chains to minimize the surface free energy of the polymer.[78−83] The surface free energy of C18 side chains is 21.6 mJ·m^{-2}, which is much lower than that of IIR and PC18A, 33.6 and 32.8 mJ·m^{-2}, respectively.[84−86] This suggests that IIR and the backbone of PC18A are aligned toward the bulk c-IPN, while C18 side chains are exposed to the air. The surface enrichment of C18 side chains above T_m can also be expected due to their greater flexibility as compared IIR and PC18A. After damaging the specimen followed by heating the damaged area above T_m, C18 side chains are thus oriented away from the bulk c-IPN phase toward the newly generated c-IPN/air interface. After bringing the damaged surfaces together, C18 side chains covering them rapidly reassociate and reform the alkyl crystals upon cooling. This explanation was also supported by elemental mapping of C and O in the healed region (Figures 9b and S10). Carbon atoms, that is, alkyl chains, dominate the cut region, while O atoms of acrylate groups are rarely seen, indicating the formation of alkyl bridges between the surfaces. The slow healing process occurs via interdiffusion of the polymer chains in the bulk phase to provide a complete healing.[39] As discussed above, the cross-link density of c-IPNs in the melt state is 2 orders of magnitude lower than that in the semicrystalline state (Figure 7d). Thus, the alkyl crystals hindering the motion of the polymer chains melt at the healing temperature, so that the high mobility of the chains facilitates side-by-side packing of C18 side chains to recover the virgin crystalline order in the c-IPNs. Moreover, as explained in Section 2.4, the contribution of elastically effective chemical cross-links to the total cross-link density of c-IPNs is less than 0.1%, and this suggests the existence of network defects such as cyclization reactions[87] and grafts PC18A chains attached at one end to the IIR backbone. Such relatively mobile graft chains with free ends may also contribute to the healing behavior of c-IPNs at elevated temperatures.[88,89]

Cut-and-heal tests were conducted to quantify macroscopic healing of IIR/PC18A c-IPNs. After 1 h healing time at 65 °C, the healing efficiency with respect to the modulus was 50 ± 2% for the IIR/PC18A with 20 wt % IIR, which increased to 92 ± 2% after 24 h of healing at the same temperature (Figure S11). Figure 10a shows typical stress−strain curves of virgin (solid curves) and healed IIR/PC18A specimens (dashed curves) by heating at 65 °C for 24 h. Healing efficiencies ε_h with respect to the modulus E, toughness W, and fracture strain ε_f are compiled in Figure 10b as a function of IIR content of c-IPNs. The healing efficiency ε_h with respect to the modulus is above 90% for all c-IPNs, while that with respect to the toughness and fracture strain increases from around 60 to 84% with increasing IIR content from 20 to 40 wt % (Table S2).

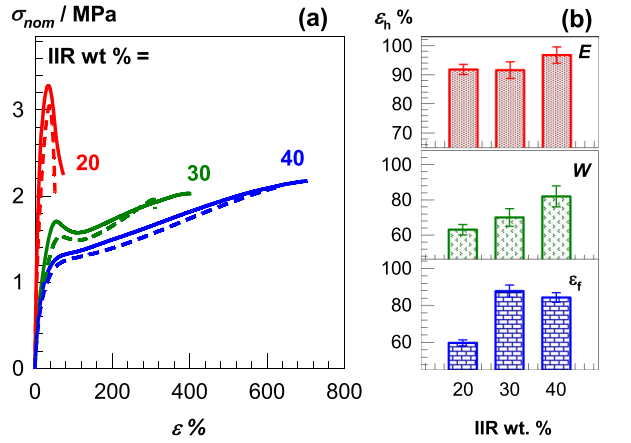

Figure 10. (a) Stress−strain curves of virgin (solid curves) and healed (dashed curves) IIR/PC18A with various IIR contents. Healing was conducted by heating at 65 °C for 24 h. (b) Healing efficiencies ε_h with respect to the modulus E, toughness W, and fracture strain ε_f plotted against IIR content of c-IPNs.

IIR/PC18A with and without C12M also exhibited shape-memory behavior due to the existence of hydrophobic associations and chemical cross-links determining their permanent shapes and alkyl crystals acting as switching segments. The images in Figure 11a demonstrate blooming of a flower-shaped IIR/PC18A specimen with 30 wt % IIR within 15 s, where alkyl crystals as switching segments fix the temporary closed flower shape, while hydrophobic associations and chemical cross-links acting as the net points determine the permanent shape of the flower after blooming. The bloom process is triggered by heating at 50 °C (see Supporting Information Movie). Bending tests were conducted to quantify shape-recovery efficiency R_θ of IIR/PC18A c-IPNs. Figure 11b showing the temperature dependence of R_θ reveals a complete shape-recovery in a narrow range of temperature (49−52 °C) for all c-IPNs.

The synthetic strategy presented here to fabricate highly tough and smart IIR/PC18A c-IPNs is suitable for a variety of n-alkyl acrylates and rubbers. Several n-alkyl (meth)acrylate monomers denoted by CxR were utilized for preparing IIR/PCxR c-IPNs with 20 wt % IIR, where Cx stands for the carbon numbers of the side chain and R = A or M for acrylates and methacrylates, respectively (Supporting Information, Text T2). The melting temperatures T_m, degree of crystallinity f_{cry}, and mechanical properties of the c-IPNs could be adjusted by changing the number of carbon atoms in the side chain. For instance, replacing C18A with the C14A monomer decreased T_m and f_{cry} of the resulting c-IPNs from 51 to 24 °C and from 0.24 to 0.17, respectively, while the toughness W increased from 1.9 to 6.3 MJ·m^{-3} (Figure S12). Moreover, as compared to the semicrystalline IIR/PC16A, the corresponding IIR/PC16M formed using the methacrylate C16M monomer is amorphous, which is attributed to the limited flexibility of methacrylate backbones hindering alignment of the alkyl side chains.[65,90] Preliminary experiments also showed that natural rubber (NR), *cis*-butadiene rubber (BR), and styrene-butadiene rubber (SBR) are soluble in the C18A monomer at 80 °C to form homogeneous mixtures. UV polymerization of the mixtures containing 20 wt % rubber at 30 ± 2 °C leads to the formation of NR/PC18A, BR/PC18A, and SBR/PC18A c-IPNs with T_m's of around 50 °C.

https://doi.org/10.1021/acsami.1c03814
ACS Appl. Mater. Interfaces 2021, 13, 21786−21799

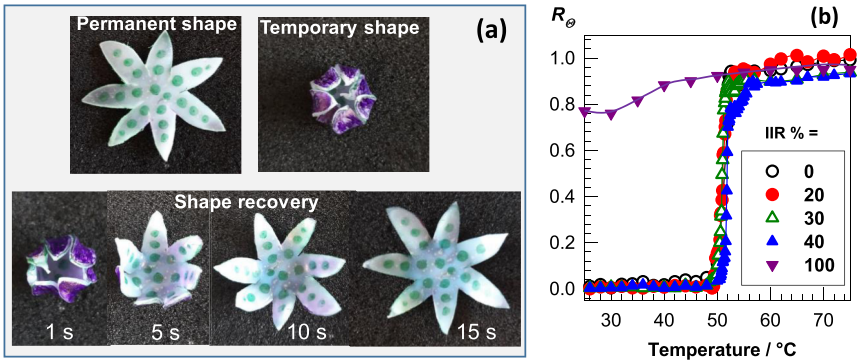

Figure 11. (a) Images of an IIR/PC18A specimen with 30 wt % IIR in permanent and temporary shapes and shape-recovery within 15 s. The green spots on the specimen were created by pipetting an aqueous fluorescein solution on its surface which forms green droplets due to its hydrophobicity. (b) Shape-recovery efficiency R_θ estimated by the bending tests plotted against the temperature for c-IPNs with various IIR contents and PC18A.

3. CONCLUSIONS

A simple and versatile strategy was presented for the preparation of highly tough and highly stretchable IIR/PC18A c-IPNs with thermally induced self-healing and shape-memory functions. Solvent-free UV polymerization of the melt mixture composed of IIR, C18A, and Irgacure 2959 at 30 ± 2 °C leads to the formation of c-IPNs containing alkyl crystals formed by side-by-side packed C18 side chains with a thickness of around 7.9 nm. The crystalline domains with a T_m of 51−52 °C are responsible for more than 99% of effective cross-links in the c-IPNs with the rest being hydrophobic associations and chemical cross-links. IIR/PC18A c-IPNs exhibit sea-island or co-continuous morphologies depending on their IIR contents. This change in the morphology is attributed to the increasing viscosity of the melt mixture before polymerization with increasing IIR content. IIR/PC18A c-IPNs exhibit a varying stiffness (9−34 MPa) and stretchability (72−740%) that can be tuned by varying IIR/PC18A weight ratio. They also exhibit a significantly higher toughness (1.9−12 MJ·m^{-3}) than their individual components which is attributed to the lamellar crystals serving as sacrificial bonds to dissipate energy and to the ductile amorphous network keeping the structure together. The properties of IIR/PC18A c-IPNs could also be tuned by incorporating the non-crystallizable hydrophobic C12M monomer in the melt mixture. IIR/PC18A c-IPNs exhibit a two-step healing process with >90% healing efficiency with respect to the modulus and a complete shape-recovery ratio induced by heating above T_m of alkyl crystals. The temperature-induced healing occurs via a quick step where C18 bridges form between the damaged surfaces followed by a slow step controlled by the interdiffusion of C18A segments in the bulk. We also show that our strategy is suitable for a variety of rubbers and *n*-alkyl (meth)acrylates of various side-chain lengths. The strategy developed here provides the design of shape-memory materials in various permanent shapes for the preparation of self-healable smart wires, tubing, rods, coatings, or films in numerous applications, including aerospace, temperature sensors, biomedical devices, and actuators.

4. EXPERIMENTAL SECTION

4.1. Materials. Butyl rubber (IIR, BK-1675N, molecular weight 180,000 g·mol^{-1}, Nizhnekamskneftekhim, Russia) was purified by dissolving in toluene and then precipitating in an excess of methanol followed by drying under vacuum to constant mass. The unsaturation degree of IIR was 1.7 ± 0.2 mol %, as determined by ^{1}H and ^{13}C NMR analysis on an Agilent VNMRS 500 MHz spectrometer (Figure S13). *n*-Octadecyl acrylate (C18A) and 2-hydroxy-4′-(2-hydroxyethoxy)-2-methylpropiophenone (Irgacure 2959) both purchased from Sigma-Aldrich (St. Louis, MO) were used without purification.

4.2. Preparation of IIR/PC18A c-IPNs. Cross-linking of IIR was conducted by melt-mixing of the reaction components IIR, C18A, and Irgacure 2959 followed by keeping the homogeneous mixture under UV light at 360 nm for 1 h. A typical cross-linking procedure to produce a c-IPN with 30 wt % IIR content involves dissolving 1.5 g of IIR in 3.5 g of C18A at 80 °C for 8 h to obtain a homogeneous viscous mixture. After the addition of 7 mg of Irgacure 2959 (0.2 wt % with respect to C18A) under stirring, the viscous mixture was cast between glass plates separated by a 1 mm spacer. After running the polymerization for 1 h at 30 ± 2 °C under UV light, a self-healable IIR/PC18A c-IPN with shape-memory function was obtained. IIR/PC18A-C12M c-IPNs were prepared as described above except that the C12M monomer was also included into the melt mixture. In this set of experiments, IIR content of the mixture was fixed at 20 wt %, while the mole fraction of C12M in the C18A + C12M mixture (x_{C12M}) was varied between 0 and 0.50 (Table S1). To estimate the molecular weight of the PC18A component of c-IPNs, UV polymerization of C18A was conducted under the same experimental condition but in the absence of IIR. Using GPC analysis, the number-average molecular weight was determined as 90,000 g·mol^{-1} with a very broad polydispersity index of 20 (see Supporting Information, Text T3). This is likely due to phase separation of PC18A at the reaction temperature which is below its melting temperature.

4.3. Characterization. XRD data were collected at 23 ± 2 °C in the angular range 2θ = 1−50° with a scan rate of 0.05°·s^{-1} on a Panalytical Empyrean instrument using CuK$_\alpha$ radiation (λ = 0.154 nm) operating at 40 kV/50 mA. SAXS data were collected at 23 °C with an exposure time of 900 s using the HECUS-SWAXS system (Graz, Austria). Nickel-filtered Cu Kα radiation (λ = 0.154 nm) operating at 50 kV/40 mA was used as the X-ray source. FTIR spectra were recorded on a Carry 630 FTIR spectrometer with ATR accessory (Agilent Technologies) over the range of 400−4000 cm^{-1}. DSC experiments were carried out on a PerkinElmer Diamond DSC under a nitrogen atmosphere. The specimens were sealed in aluminum pans and scanned between 5 and 80 °C with a scanning rate of 5 °C·min^{-1}. The fraction f_{cry} of C18A units in crystalline domains was calculated by $f_{cry} = w_{C18A}\,\Delta H_m/\Delta H_m^o$, where w_{C18A} is the mass fraction of C18A in the specimen and ΔH_m and ΔH_m° are the melting enthalpies (in J·g^{-1}) of the specimen and crystalline C18A units, respectively, where the latter was taken as 219.4 J·g^{-1}.[91,92] For transmission (TEM) and STEM analysis, ultrathin sections (~40 nm-thick) of the c-IPNs were prepared using a cryo-ultramicrotome (RMC PowerTome-PC, Boeckeler Instruments) with a diamond knife (Diatome) at −150 °C. The sections were then collected on 200-mesh lacy carbon-coated copper grids (Ted Pella) and stained with

https://doi.org/10.1021/acsami.1c03814
ACS Appl. Mater. Interfaces 2021, 13, 21786−21799

Uranless for about 1 min. The images of unstained and stained c-IPNs were obtained with a JEOL ARM-200CF instrument in both TEM and STEM modes operated at 200 kV. The BF mode was also used to increase the contrast of the images, and they were recorded with a Gatan Orius SC200D CCD camera. Energy-dispersive X-ray spectroscopy (EDX) was used in the STEM mode to provide elemental analysis for carbon and oxygen. The average size of the dispersed particles in the TEM images was estimated by analyzing at least 110 particles in the images taken at various magnifications. The apparent particle size was calculated as $d = (4A/\pi)^{0.5}$, where A is the area of an individual particle. The number and weight averages of the particle sizes were estimated as $d_n = \sum n_i d_i / \sum n_i$ and $d_w = \sum n_i d_i 2 / \sum n_i d_i$, respectively, where n_i is the number of particles within a specified range about the value d_i.

Rheological measurements of cylindrical specimens (20 mm in diameter and ∼1 mm in thickness) were conducted between the parallel plates of a Gemini 150 rheometer system (Bohlin Instruments) combined with a Peltier device to control temperature. The upper plate (diameter 20 mm) was fixed at a distance of 1050 ± 85 μm depending on the specimen thickness. The storage modulus G' and loss modulus G'' were monitored by changing the temperature between below and above the melting temperature of the c-IPNs at a frequency ω of 6.3 rad·s^{-1} and a deformation amplitude γ_o of 0.1%. For this purpose, the specimens were first kept at 65 °C and then cooled down to 25 °C at a rate of 2 °C·min^{-1}. Frequency sweep tests were carried out at both 25 and 65 °C over the frequency range 0.3−300 rad·s^{-1}.

The mechanical properties of c-IPNs were determined at 23 ± 2 °C by uniaxial tensile tests on a Zwick Roell test machine with a 500 N load cell. The flat specimens of 20 × 30 × 1 mm in dimensions were fixed between the top and bottom grips at a fixed initial length between jaws of 10 mm and then stretched until complete failure at a rate of 5 min^{-1}. The nominal stress σ_{nom} and strain ε data were recorded where σ_{nom} is the force per cross-sectional area of the undeformed sample and ε is the change in the sample length relative to its initial length. Young's modulus E was calculated from the slope of the stress−strain curves between 0.01 and 2% deformations. Cyclic mechanical tests were carried out at the same strain rate by conducting five successive loading and unloading steps on the specimens to a maximum strain of 70% without a waiting time between cycles. The mechanical cycles were characterized by the hysteresis energy U_{hys}, the area surrounded by the loading and unloading curves, and by the hysteresis energy per loading energy f_{diss} (Figure S7c).

Self-healing behavior of c-IPNs was investigated by optical microscopy, confocal microscopy, SEM−EDX mapping, and mechanical testing. For optical microscopy measurements, a cut of around 70 μm in diameter was first created on a cylindrical specimen with a thickness of 1 mm using a blade. The specimen was then heated at 65 °C, and the change in the cut diameter was monitored using an image analyzing system consisting of a XSZ single zoom microscope, a CDD digital camera (TK 1381EG), and a PC with the Image-Pro Plus data analyzing system. A true color confocal microscope (Zeiss, AXIO, CSM 700) was also used to monitor the healing of the cut area as a function of time. In addition, healing of around 15 μm thick cut at 50 °C was monitored using scanning electron microscopy (SEM) images that were recorded on an FEI Quanta FEG 250 microscope (Hillsboro, OR, USA) equipped with an EDX at an accelerating voltage of 20 kV. For mechanical testing, the specimens of dimensions 10 × 30 × 1 mm were first cut in the middle into two equally sized pieces and then healed by keeping the cut surfaces in contact for 24 h at 65 °C. The mechanical properties of virgin and healed c-IPNs were determined by uniaxial mechanical testing.

The shape-memory behavior was studied by a bending test as follows: The flat specimen of 20 × 30 × 1 mm in dimension is folded at 65 °C and then cooled to 25 °C to keep the deformed temporary shape. The specimen is then heated from 25 to 75 °C at 1−3 °C steps during which the deformation angle θ_d is monitored using the image analyzing system detailed above. The shape-recovery ratio R_θ was calculated as $R_\theta = \theta_d/180$.

The swelling ratio of c-IPNs was determined by immersing flat specimens (dimensions: 4 cm × 5 cm × ∼1 mm) in toluene for at least 2 weeks during which toluene was refreshed every other day. After transferring into methanol, they were dried under vacuum to constant mass. The equilibrium weight swelling ratio q_w of c-IPNs in toluene was calculated as $q_w = m_s/m_{dry}$, where m_s and m_{dry} are the masses of the specimen after swelling in toluene and after drying, respectively.

■ ASSOCIATED CONTENT

Supporting Information

The Supporting Information is available free of charge at https://pubs.acs.org/doi/10.1021/acsami.1c03814.

Details on material preparation, NMR, FTIR, DSC, SEM−EDX, and viscosity data, and mechanical test results (PDF)

Shape-memory behavior of c-IPNs (MP4)

■ AUTHOR INFORMATION

Corresponding Author

Oguz Okay − *Department of Chemistry, Istanbul Technical University, 34469 Maslak, Istanbul, Turkey;* orcid.org/0000-0003-2717-4150; Phone: +90 212 285 3156; Email: okayo@itu.edu.tr

Authors

Esra Su − *Department of Chemistry, Istanbul Technical University, 34469 Maslak, Istanbul, Turkey*

Cigdem Bilici − *Department of Chemistry, Istanbul Technical University, 34469 Maslak, Istanbul, Turkey*

Gozde Bayazit − *Department of Physics Engineering, Hacettepe University, 06800 Beytepe, Ankara, Turkey*

Semra Ide − *Department of Physics Engineering and Department of Nanotechnology and Nanomedicine, Hacettepe University, 06800 Beytepe, Ankara, Turkey*

Complete contact information is available at: https://pubs.acs.org/10.1021/acsami.1c03814

Author Contributions

The manuscript was written through contributions of all authors. All authors have given approval to the final version of the manuscript.

Funding

This work was supported by the Scientific and Technical Research Council of Turkey (TUBITAK), MAG-218M502. O.O. thanks the Turkish Academy of Sciences (TUBA) for the partial support.

Notes

The authors declare no competing financial interest.

■ REFERENCES

(1) Santana, M. H.; den Brabander, M.; García, S.; van der Zwaag, S. Routes to Make Natural Rubber Heal: A Review. *Polym. Rev.* **2018**, *58*, 585−609.

(2) Behl, M.; Lendlein, A.; Lendlein, A. Shape-Memory Polymers and Shape-Changing Polymers. *Shape-Memory Polymers*; Advances in Polymer Science; Springer, 2010; Vol. *226*, pp 1−40.

(3) Cordier, P.; Tournilhac, F.; Soulié-Ziakovic, C.; Leibler, L. Self-Healing and Thermoreversible Rubber from Supramolecular Assembly. *Nature* **2008**, *451*, 977−980.

(4) Wang, D.; Guo, J.; Zhang, H.; Cheng, B.; Shen, H.; Zhao, N.; Xu, J. Intelligent Rubber with Tailored Properties for Self-Healing and Shape Memory. *J. Mater. Chem. A* **2015**, *3*, 12864−12872.

(5) Wu, J.; Cai, L.-H.; Weitz, D. A. Tough Self-Healing Elastomers by Molecular Enforced Integration of Covalent and Reversible Networks. *Adv. Mater.* **2017**, *29*, 1702616.
(6) Maes, F.; Montarnal, D.; Cantournet, S.; Tournilhac, F.; Corté, L.; Leibler, L. Activation and Deactivation of Self-Healing in Supramolecular Rubbers. *Soft Matter* **2012**, *8*, 1681−1687.
(7) Chen, Y.; Kushner, A. M.; Williams, G. A.; Guan, Z. Multiphase Design of Autonomic Self-Healing Thermoplastic Elastomers. *Nat. Chem.* **2012**, *4*, 467−472.
(8) Burattini, S.; Greenland, B. W.; Merino, D. H.; Weng, W.; Seppala, J.; Colquhoun, H. M.; Hayes, W.; Mackay, M. E.; Hamley, I. W.; Rowan, S. J. A Healable Supramolecular Polymer Blend Based on Aromatic π-π Stacking and Hydrogen-Bonding Interactions. *J. Am. Chem. Soc.* **2010**, *132*, 12051−12058.
(9) Sordo, F.; Mougnier, S.-J.; Loureiro, N.; Tournilhac, F.; Michaud, V. Design of Self-Healing Supramolecular Rubbers with a Tunable Number of Chemical Cross-Links. *Macromolecules* **2015**, *48*, 4394−4402.
(10) Kang, J.; Son, D.; Wang, G. N.; Liu, Y.; Lopez, J.; Kim, Y.; Oh, J. Y.; Katsumata, T.; Mun, J.; Lee, Y.; Jin, L.; Tok, J. B.; Bao, Z. Tough and Water-Insensitive Self-Healing Elastomer for Robust Electronic Skin. *Adv. Mater.* **2018**, *30*, 1706846.
(11) Zhang, L.; Liu, Z.; Wu, X.; Guan, Q.; Chen, S.; Sun, L.; Guo, Y.; Wang, S.; Song, J.; Jeffries, E. M.; He, C.; Qing, F. L.; Bao, X.; You, Z. A Highly Efficient Self-Healing Elastomer with Unprecedented Mechanical Properties. *Adv. Mater.* **2019**, *31*, 1901402.
(12) Montarnal, D.; Tournilhac, F.; Hidalgo, M.; Couturier, J.-L.; Leibler, L. Versatile One-Pot Synthesis of Supramolecular Plastics and Self-Healing Rubbers. *J. Am. Chem. Soc.* **2009**, *131*, 7966−7967.
(13) Wu, Y.; Hu, J.; Han, J.; Zhu, Y.; Huang, H.; Li, J.; Tang, B. Two-Way Shape Memory Polymer with "Switch−Spring" Composition by Interpenetrating Polymer Network. *J. Mater. Chem. A* **2014**, *2*, 18816.
(14) Kuang, X.; Chen, K.; Dunn, C. K.; Wu, J.; Li, V. C. F.; Qi, H. J. 3D Printing of Highly Stretchable, Shape-Memory, and Self-Healing Elastomer toward Novel 4D Printing. *ACS Appl. Mater. Interfaces* **2018**, *10*, 7381−7388.
(15) Xiang, H. P.; Qian, H. J.; Lu, Z. Y.; Rong, M. Z.; Zhang, M. Q. Crack Healing and Reclaiming of Vulcanized Rubber by Triggering the Rearrangement of Inherent Sulfur Crosslinked Networks. *Green Chem.* **2015**, *17*, 4315−4325.
(16) Xiang, H. P.; Rong, M. Z.; Zhang, M. Q. Self-Healing, Reshaping, and Recycling of Vulcanized Chloroprene Rubber: A Case Study of Multitask Cyclic Utilization of Cross-Linked Polymer. *ACS Sustainable Chem. Eng.* **2016**, *4*, 2715−2724.
(17) Hernández, M.; Grande, A. M.; Dierkes, W.; Bijleveld, J.; van der Zwaag, S.; García, S. J. Turning Vulcanized Natural Rubber into a Self-Healing Polymer: Effect of the Disulfide/Polysulfide Ratio. *ACS Sustainable Chem. Eng.* **2016**, *4*, 5776−5784.
(18) Hernández, M.; Grande, A. M.; van der Zwaag, S.; García, S. J. Monitoring Network and Interfacial Healing Processes by Broadband Dielectric Spectroscopy: A Case Study on Natural Rubber. *ACS Appl. Mater. Interfaces* **2016**, *8*, 10647−10656.
(19) Rahman, M. A.; Sartore, L.; Bignotti, F.; Di Landro, L. Autonomic Self-Healing in Epoxidized Natural Rubber. *ACS Appl. Mater. Interfaces* **2013**, *5*, 1494−1502.
(20) Huang, J.; Cao, L.; Yuan, D.; Chen, Y. Design of Novel Self-Healing Thermoplastic Vulcanizates Utilizing Thermal/Magnetic/Light-Triggered Shape Memory Effects. *ACS Appl. Mater. Interfaces* **2018**, *10*, 40996−41002.
(21) Kuang, X.; Liu, G.; Dong, X.; Wang, D. Enhancement of Mechanical and Self-Healing Performance in Multiwall Carbon Nanotube/Rubber Composites via Diels-Alder Bonding. *Macromol. Mater. Eng.* **2016**, *301*, 535−541.
(22) Abd Rabo Moustafa, M. M.; Gillies, E. R. Rubber Functionalization by Diels−Alder Chemistry: From Cross-Linking to Multifunctional Graft Copolymer Synthesis. *Macromolecules* **2013**, *46*, 6024−6030.
(23) Tanasi, P.; Hernández Santana, M.; Carretero-González, J.; Verdejo, R.; López-Manchado, M. A. Thermo-Reversible Crosslinked Natural Rubber: A Diels-Alder Route for Reuse and Self-Healing Properties in Elastomers. *Polymer* **2019**, *175*, 15−24.
(24) Feng, Z.; Hu, J.; Zuo, H.; Ning, N.; Zhang, L.; Yu, B.; Tian, M. Photothermal-Induced Self-Healable and Reconfigurable Shape Memory Bio-Based Elastomer with Recyclable Ability. *ACS Appl. Mater. Interfaces* **2019**, *11*, 1469−1479.
(25) Xu, C.; Cui, R.; Fu, L.; Lin, B. Recyclable and Heat-Healable Epoxidized Natural Rubber/Bentonite Composites. *Compos. Sci. Technol.* **2018**, *167*, 421−430.
(26) Cheng, B.; Lu, X.; Zhou, J.; Qin, R.; Yang, Y. Dual Cross-Linked Self-Healing and Recyclable Epoxidized Natural Rubber Based on Multiple Reversible Effects. *ACS Sustainable Chem. Eng.* **2019**, *7*, 4443−4455.
(27) Cao, L.; Yuan, D.; Xu, C.; Chen, Y. Biobased, Self-Healable, High Strength Rubber with Tunicate Cellulose Nanocrystals. *Nanoscale* **2017**, *9*, 15696−15706.
(28) Schüssele, A. C.; Nübling, F.; Thomann, Y.; Carstensen, O.; Bauer, G.; Speck, T.; Mülhaupt, R. Self-Healing Rubbers Based on NBR Blends with Hyperbranched Polyethylenimines. *Macromol Mater. Eng.* **2012**, *297*, 411−419.
(29) Das, A.; Sallat, A.; Böhme, F.; Suckow, M.; Basu, D.; Wießner, S.; Stöckelhuber, K. W.; Voit, B.; Heinrich, G. Ionic Modification Turns Commercial Rubber into a Self-Healing Material. *ACS Appl. Mater. Interfaces* **2015**, *7*, 20623−20630.
(30) Suckow, M.; Mordvinkin, A.; Roy, M.; Singha, N. K.; Heinrich, G.; Voit, B.; Saalwächter, K.; Böhme, F. Tuning the Properties and Self-Healing Behavior of Ionically Modified Poly(isobutylene-co-isoprene) Rubber. *Macromolecules* **2018**, *51*, 468−479.
(31) Mordvinkin, A.; Suckow, M.; Böhme, F.; Colby, R. H.; Creton, C.; Saalwächter, K. Hierarchical Sticker and Sticky Chain Dynamics in Self-Healing Butyl Rubber Ionomers. *Macromolecules* **2019**, *52*, 4169−4184.
(32) Xu, C.; Cao, L.; Lin, B.; Liang, X.; Chen, Y. Design of Self-Healing Supramolecular Rubbers by Introducing Ionic Cross-Links into Natural Rubber via a Controlled Vulcanization. *ACS Appl. Mater. Interfaces* **2016**, *8*, 17728−17737.
(33) Xu, C.; Cao, L.; Huang, X.; Chen, Y.; Lin, B.; Fu, L. Self-Healing Natural Rubber with Tailorable Mechanical Properties Based on Ionic Supramolecular Hybrid Network. *ACS Appl. Mater. Interfaces* **2017**, *9*, 29363−29373.
(34) Xu, C.; Huang, X.; Li, C.; Chen, Y.; Lin, B.; Liang, X. Design of "Zn2+ Salt-Bondings" Cross-Linked Carboxylated Styrene Butadiene Rubber with Reprocessing and Recycling Ability via Rearrangements of Ionic Cross-Linkings. *ACS Sustainable Chem. Eng.* **2016**, *4*, 6981−6990.
(35) Lai, S.-M.; Liu, J.-L.; Huang, Y.-H. Preparation of Self-Healing Natural Rubber/Polycaprolactone (NR/PCL) Blends. *J. Macromol. Sci., Part B: Phys.* **2020**, *59*, 587−607.
(36) Cao, Y.; Tan, Y. J.; Li, S.; Lee, W. W.; Guo, H.; Cai, Y.; Wang, C.; Tee, B. C.-K. Self-Healing Electronic Skins for Aquatic Environments. *Nat. Electron.* **2019**, *2*, 75−82.
(37) Chang, Y.-W. Shape-Memory Polymer Blends. In *Functional Polymer Blends*; Mittal, V., Ed.; Synthesis, Properties, and Performance; CRC, Taylor & Francis Group: Boca Raton, 2012; pp 127−146.
(38) Yu, K.; Xin, A.; Feng, Z.; Lee, K. H.; Wang, Q. Mechanics of Self-Healing Thermoplastic Elastomers. *J. Mech. Phys. Solids* **2020**, *137*, 103831.
(39) Montano, V.; Wempe, M. M. B.; Does, S. M. H.; Bijleveld, J. C.; van der Zwaag, S.; Garcia, S. J. Controlling Healing and Toughness in Polyurethanes by Branch-Mediated Tube Dilation. *Macromolecules* **2019**, *52*, 8067−8078.
(40) Xu, C.; Nie, J.; Wu, W.; Zheng, Z.; Chen, Y. Self-Healable, Recyclable, and Strengthened Epoxidized Natural Rubber/Carboxymethyl Chitosan Biobased Composites with Hydrogen Bonding Supramolecular Hybrid Networks. *ACS Sustainable Chem. Eng.* **2019**, *7*, 15778−15789.

https://doi.org/10.1021/acsami.1c03814
ACS Appl. Mater. Interfaces 2021, 13, 21786−21799

(41) Le, H. H.; Hait, S.; Das, A.; Wiessner, S.; Stoeckelhuber, K. W.; Boehme, F.; Uta Reuter, U.; Naskar, K.; Heinrich, G.; Radusch, H.-J. Self-Healing Properties of Carbon Nanotube Filled Natural Rubber/Bromobutyl Rubber Blends. *eXPRESS Polym. Lett.* **2017**, *11*, 230−242.
(42) Brostowitz, N. R.; Weiss, R. A.; Cavicchi, K. A. Facile Fabrication of a Shape Memory Polymer by Swelling Cross-Linked Natural Rubber with Stearic Acid. *ACS Macro Lett.* **2014**, *3*, 374−377.
(43) Platé, N. A.; Shibaev, V. P. Comb-Like Polymers: Structure and Properties. *J. Polym. Sci. Macromol. Rev.* **1974**, *8*, 117−253.
(44) Inomata, K.; Sakamaki, Y.; Nose, T.; Sasaki, S. Solid-State Structure of Comb-Like Polymers having n-Octadecyl Side Chains II. Crystalline-Amorphous Layered Structure. *Polymer J.* **1996**, *28*, 992−999.
(45) O'Leary, K. A.; Paul, D. R. Physical Properties of Poly(n-alkyl acrylate) Copolymers. Part 1. Crystalline/Crystalline Combinations. *Polymer* **2006**, *47*, 1226−1244.
(46) O'Leary, K. A.; Paul, D. R. Physical Properties of Poly(n-alkyl acrylate) Copolymers. Part 2. Crystalline/Non-Crystalline Combinations. *Polymer* **2006**, *47*, 1245−1258.
(47) Kirkland, B. S.; Paul, D. R. Gas Transport in Poly(n-alkyl acrylate)/poly(m-alkyl acrylate) Blends. *Polymer* **2008**, *49*, 507−524.
(48) Wang, S.; Robertson, M. L. Thermodynamic Interactions between Polystyrene and Long-Chain Poly(n-alkyl acrylates) Derived from Plant Oils. *ACS Appl. Mater. Interfaces* **2015**, *7*, 12109−12118.
(49) Matsuda, A.; Sato, J.; Yasunaga, H.; Osada, Y. Order-Disorder Transition of a Hydrogel Containing an n-Alkyl Acrylate. *Macromolecules* **1994**, *27*, 7695−7698.
(50) Osada, Y.; Matsuda, A. Shape Memory in Hydrogels. *Nature* **1995**, *376*, 219.
(51) Lee, J. L.; Pearce, E. M.; Kwei, T. K. Morphological Development in Alkyl-Substituted Semiflexible Polymers. *Macromolecules* **1997**, *30*, 8233−8244.
(52) Bilici, C.; Okay, O. Shape Memory Hydrogels via Micellar Copolymerization of Acrylic Acid and n-Octadecyl Acrylate in Aqueous Media. *Macromolecules* **2013**, *46*, 3125−3131.
(53) Ebata, K.; Hashimoto, Y.; Yamamoto, S.; Mitsuishi, M.; Nagano, S.; Matsui, J. Nanophase Separation of Poly(N-alkyl acrylamides): The Dependence of the Formation of Lamellar Structures on their Alkyl Side Chains. *Macromolecules* **2019**, *52*, 9773−9780.
(54) Bilici, C.; Can, V.; Nöchel, U.; Behl, M.; Lendlein, A.; Okay, O. Melt-Processable Shape-Memory Hydrogels with Self-Healing Ability of High Mechanical Strength. *Macromolecules* **2016**, *49*, 7442−7449.
(55) Okay, O. Semicrystalline Physical Hydrogels with Shape-Memory and Self-Healing Properties. *J. Mater. Chem. B* **2019**, *7*, 1581−1596.
(56) Fei, P.; Cavicchi, K. A. Synthesis and Characterization of a Poly(styrene-block-methylacrylate-random-octadecylacrylate-block-styrene) Shape Memory ABA Triblock Copolymer. *ACS Appl. Mater. Interfaces* **2010**, *2*, 2797−2803.
(57) Wang, S.; Vajjala Kesava, S.; Gomez, E. D.; Robertson, M. L. Sustainable Thermoplastic Elastomers Derived from Fatty Acids. *Macromolecules* **2013**, *46*, 7202−7212.
(58) Agirre, A.; Heras-Alarcón, C. d. l.; Wang, T.; Keddie, J. L.; Asua, J. M. Waterborne, Semicrystalline, Pressure-Sensitive Adhesives with Temperature-Responsiveness and Optimum Properties. *ACS Appl. Mater. Interfaces* **2010**, *2*, 443−451.
(59) Puskas, J. E.; Chen, Y.; Dahman, Y.; Padavan, D. Polyisobutylene-Based Biomaterials. *J. Polym. Sci., Part A: Polym. Chem.* **2004**, *42*, 3091−3109.
(60) Okay, O.; Durmaz, S.; Erman, B. Solution Cross-Linked Poly(isobutylene) Gels: Synthesis and Swelling Behavior. *Macromolecules* **2000**, *33*, 4822−4827.
(61) Puskas, J. E.; Chen, Y. Biomedical Application of Commercial Polymers and Novel Polyisobutylene-Based Thermoplastic Elastomers for Soft Tissue Replacement. *Biomacromolecules* **2004**, *5*, 1141−1154.
(62) Song, B. G.; Lee, D. C. Dilute Solution Properties and Molecular Conformation of Poly(n-octadecyl acrylate). *Polymer* **1986**, *10*, 588−598.
(63) Wang, J.; Wu, J.; Luo, Y.; Zhang, Y.; Guo, S.; Pan, S. Peroxide Crosslinked Butyl Rubber Composites using TEMPO and Sorbates. *Compos. Sci. Technol.* **2019**, *183*, 107805.
(64) Mierzwa, M.; Floudas, G.; Štepánek, P.; Wegner, G. Effect of Pressure on the Side-Chain Crystallization of Poly(n-octadecyl methacrylate) Studied by Dielectric Spectroscopy. *Phys. Rev. B: Condens. Matter Mater. Phys.* **2000**, *62*, 14012−14019.
(65) Tuncaboylu, D. C.; Argun, A.; Sahin, M.; Sari, M.; Okay, O. Structure Optimization of Self-Healing Hydrogels Formed via Hydrophobic Interactions. *Polymer* **2012**, *53*, 5513−5522.
(66) John, J.; Suriyakala, R.; Thomas, S.; Mendez, J. M.; Pius, A.; Thomas, S. Morphology, Mechanical and Thermal Properties of Nano-Structured full IPNs Based on Polyisoprene and PMMA. *J. Mater. Sci.* **2010**, *45*, 2892−2901.
(67) Guo, H.; Zhang, Y.; Xue, F.; Cai, Z.; Shang, Y.; Li, J.; Chen, Y.; Wu, Z.; Jiang, S. In-situ Synchrotron SAXS and WAXS Investigations on Deformation and $\alpha-\beta$ Transformation of Uniaxial Stretched Poly(vinylidene fluoride). *CrystEngComm* **2013**, *15*, 1597−1606.
(68) Humbert, S.; Lame, O.; Chenal, J.-M.; Rochas, C.; Vigier, G. Small Strain Behavior of Polyethylene: In situ SAXS Measurements. *J. Polym. Sci., Part B: Polym. Phys.* **2010**, *48*, 1535−1542.
(69) Nitta, K.-H.; Takayanagi, M. Novel Proposal of Lamellar Clustering Process for Elucidation of Tensile Yield Behavior of Linear Polyethylenes. *J. Macromol. Sci., Part B: Phys.* **2003**, *42*, 107−126.
(70) Nitta, K.-H.; Takayanagi, M. Role of Tie Molecules in the Yielding Deformation of Isotactic Polypropylene. *J. Polym. Sci., Part B: Polym. Phys.* **1999**, *37*, 357−368.
(71) Nitta, K.-H.; Takayanagi, M. Tensile Yield of Isotactic Polypropylene in terms of a Lamellar-Cluster Model. *J. Polym. Sci., Part B: Polym. Phys.* **2000**, *38*, 1037−1044.
(72) Bilici, C.; Ide, S.; Okay, O. Yielding Behavior of Tough Semicrystalline Hydrogels. *Macromolecules* **2017**, *50*, 3647−3654.
(73) Mark, J. E.; Erman, B. *Rubberlike Elasticity*; Cambridge University Press: Cambridge, U.K., 2007.
(74) Flory, P. J. *Principles of Polymer Chemistry*; Cornell University Press: Ithaca, NY, 1953.
(75) Treloar, L. R. G. *The Physics of Rubber Elasticity*; University Press: Oxford, 1975.
(76) Yang, Y.; Wang, C.; Wiener, C. G.; Hao, J.; Shatas, S.; Weiss, R. A.; Vogt, B. D. Tough Stretchable Physically-Cross-Linked Electrospun Hydrogel Fiber Mats. *ACS Appl. Mater. Interfaces* **2016**, *8*, 22774−22779.
(77) Durmaz, S.; Fank, S.; Okay, O. Swelling and Mechanical Properties of Solution Crosslinked Poly(isobutylene) gels. *Macromol. Chem. Phys.* **2002**, *203*, 663−672.
(78) Clarke, M. L.; Chen, C.; Wang, J.; Chen, Z. Molecular Level Structures of Poly(n-alkyl methacrylate)s with Different Side Chain Lengths at the Polymer/Air and Polymer/Water Interfaces. *Langmuir* **2006**, *22*, 8800−8806.
(79) Kajiyama, T.; Tanaka, K.; Takahara, A. Surface Segregation of the Higher Surface Free Energy Component in Symmetric Polymer Blend Films. *Macromolecules* **1998**, *31*, 3746−3749.
(80) Yokoyama, H.; Miyamae, T.; Han, S.; Ishizone, T.; Tanaka, K.; Takahara, A.; Torikai, N. Spontaneously Formed Hydrophilic Surfaces by Segregation of Block Copolymers with Water-Soluble Blocks. *Macromolecules* **2005**, *38*, 5180−5189.
(81) Wang, J.; Woodcock, S. E.; Buck, S. M.; Chen, C.; Chen, Z. Different Surface-Restructuring Behaviors of Poly(methacrylate)s Detected by SFG in Water. *J. Am. Chem. Soc.* **2001**, *123*, 9470−9471.
(82) Fujimori, A. Langmuir-Blodgett (LB) Film. In *Encyclopedia of Polymeric Nanomaterials*; Kobayashi, S., Müllen, K., Eds.; Springer: Berlin, Heidelberg, 2015; pp 1044−1050.
(83) Zhang, Q.; Wang, Q.; Jiang, J.; Zhan, X.; Chen, F. Microphase Structure, Crystallization Behavior, and Wettability Properties of Novel Fluorinated Copolymers Poly(perfluoroalkyl acrylate-co-stearyl

https://doi.org/10.1021/acsami.1c03814
ACS Appl. Mater. Interfaces 2021, 13, 21786−21799

acrylate) Containing Short Perfluorohexyl Chains. *Langmuir* **2015**, *31*, 4752−4760.
(84) Wypych, G. *Handbook of Polymers*; ChemTec Publishing: Toronto, 2012.
(85) Yilbas, B. S.; Ali, H.; Al-Sharafia, A.; Al-Aqeelia, N. Reversible Exchange of Wetting State of a Hydrophobic Surface via Phase Change Material Coating. *RSC Adv.* **2018**, *8*, 938−947.
(86) Lewin, M.; Mey-Marom, A.; Frank, R. Surface Free Energies of Polymeric Materials, Additives and Minerals. *Polym. Adv. Technol.* **2005**, *16*, 429−441.
(87) Okay, O.; Kurz, M.; Lutz, K.; Funke, W. Cyclization and Reduced Pendant Vinyl Group Reactivity during the Free-radical Crosslinking Polymerization of 1,4-Divinylbenzene. *Macromolecules* **1995**, *28*, 2728−2737.
(88) Yamaguchi, M.; Ono, S.; Okamoto, K. Interdiffusion of Dangling Chains in Weak Gel and its Application to Self-Repairing Material. *Mater. Sci. Eng., B* **2009**, *162*, 189−194.
(89) Amouroux, N.; Léger, L. Effect of Dangling Chains on Adhesion Hysteresis of Silicone Elastomers, Probed by JKR Test. *Langmuir* **2003**, *19*, 1396−1401.
(90) Livshin, S.; Silverstein, M. S. Crystallinity in Cross-Linked Porous Polymers from High Internal Phase Emulsions. *Macromolecules* **2007**, *40*, 6349−6354.
(91) Mogri, Z.; Paul, D. R. Gas Sorption and Transport in Side-Chain Crystalline and Molten Poly(octadecyl acrylate). *Polymer* **2001**, *42*, 2531−2542.
(92) Bisht, H. S.; Pande, P. P.; Chatterjee, A. K. Docosyl Acrylate Modified Polyacrylic Acid: Synthesis and Crystallinity. *Eur. Polym. J.* **2002**, *38*, 2355−2358.

https://doi.org/10.1021/acsami.1c03814
ACS Appl. Mater. Interfaces 2021, 13, 21786−21799